

RESEARCH

Open Access



Dual-source powered sea urchin-like nanomotors for intravesical photothermal therapy of bladder cancer

Yixuan Mou^{1†}, Zhenghong Liu^{1†}, Wentao Xu^{2†}, Bin Zheng^{1,3}, Minghai Ma⁴, Xiaowen Qin^{1,5}, Jiajia Zheng², Ran Ni⁶, Haichang Li¹, Lei Wang⁷, Yuchen Bai¹, Jinhai Fan⁴, Xiaolong Qi¹, Qi Zhang^{1*}, Pu Zhang^{1*} and Dahong Zhang^{1*}

Abstract

Bladder cancer (BCa) ranks as the 9th most prevalent malignancy worldwide, featured by its high risk of recurrence. Intravesical therapy constitutes the most important modality to tackle BCa, but its efficiency is often compromised due to the dense physiological barriers in BCa, the instability of the catalytic environment, and the rapid clearance facilitated by periodic urination. Here, we present a dual-source powered sea urchin-like nanomotor, which feature a gold nanocore decorated with ultrasmall platinum nanoparticles and ureases, enable rapid propulsion through the catalytic conversion of abundant urea and hydrogen peroxide present in the bladder cavity and BCa microenvironment, respectively. Our dual-source powered Au-Pt@ur NPs nanoparticles translocated across the mucus barrier rapidly, deeply penetrated tumor and hence chemo-resected bladder tumors in all cases. These results hold substantial promise for the development of biocompatible nanomotors for improved BCa intravesical therapy.

[†]Yixuan Mou, Zhenghong Liu and Wentao Xu contributed equally to this work.

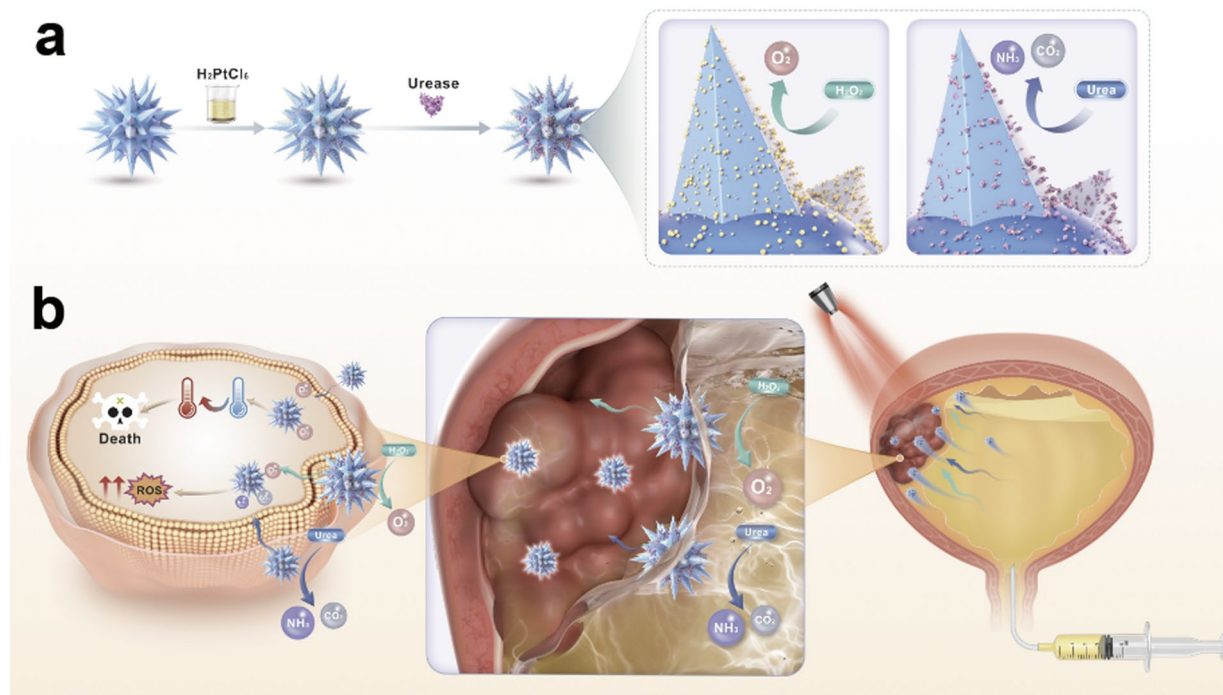
*Correspondence:

Qi Zhang
clinic@126.com
Pu Zhang
zhangpuxjtuer@163.com
Dahong Zhang
zppurology@163.com

Full list of author information is available at the end of the article



© The Author(s) 2025. **Open Access** This article is licensed under a Creative Commons Attribution-NonCommercial-NoDerivatives 4.0 International License, which permits any non-commercial use, sharing, distribution and reproduction in any medium or format, as long as you give appropriate credit to the original author(s) and the source, provide a link to the Creative Commons licence, and indicate if you modified the licensed material. You do not have permission under this licence to share adapted material derived from this article or parts of it. The images or other third party material in this article are included in the article's Creative Commons licence, unless indicated otherwise in a credit line to the material. If material is not included in the article's Creative Commons licence and your intended use is not permitted by statutory regulation or exceeds the permitted use, you will need to obtain permission directly from the copyright holder. To view a copy of this licence, visit <http://creativecommons.org/licenses/by-nc-nd/4.0/>.

Graphical abstract

Keywords Nanomotors, Dual-source powered, Bladder cancer, Photothermal therapy, Intravesical therapy

Introduction

Bladder cancer (BCa) is a prevalent malignancy, ranking as the 9th most common cancer globally, with an annual incidence of approximately 615,000 cases [1]. The management of non-muscle invasive BCa (NMIBC) is particularly challenging due to its high risk of recurrence and progression [2]. Transurethral resection of bladder tumors (TURBT) is the first-line therapy for NMIBC and the subsequent use intravesical therapy (IT) is recommended to eliminate residual and exfoliative tumors [3–4]. However, the luminal surface barrier, composed of the mucus layer and the densely packed tissue layer, is highly impermeable [5] and thus hindering the tissue-penetration of intravesical drugs.

Strategies against BCa physiological barrier can be divided into paracellular transport, transcytosis, direct transfer and self-propelled transport [6]. Self-propelled transport, a non-ATP-mediated active transport, harnesses energy from various sources. Artificial nanomotors serve as instruments to achieve self-propulsion mainly by converting chemical energy into mechanical force [7–9]. In complex real-world applications, nanomotors must navigate the viscosity and flow rate of body fluids, thus, more powerful propulsion and higher movement speed equate to enhanced

tissue-penetrating efficiency. Furthermore, the performance of single-source propulsion nanomotors is susceptible to fluctuations in the catalytic byproducts and the environmental conditions, which can lead to suboptimal power generation and compromised stability [10]. Therefore, the development of micro/nanomotors with superior power remains an ongoing challenge [11]. Dual-source powered nanomotors usually integrate two types of energy inputs, such as light [12], ultrasound [13], or chemical reactions [14] to overcome the limitations of insufficient power or limited control owned by single-source systems, thereby greatly enhancing the self-propelled motion performance and making themselves more adaptable to the real-world application.

Here, we developed a dual-source powered nanomotor, Au-Pt@ur NPs, featuring a core of gold nanoparticles (Au NPs) adorned with ultrasmall platinum (Pt) nanoparticles and ureases on its surface. Urease acts as a biocatalytic unit, facilitating the enzymatic conversion of urea to generate power for the nanomotors, while platinum engages in chemical reactions with hydrogen peroxide in the tumor microenvironment to further enhance propulsion [15–16]. Au-Pt@ur NPs showcases a sea urchin-like appearance, which can provide multifaceted advantages, including increased

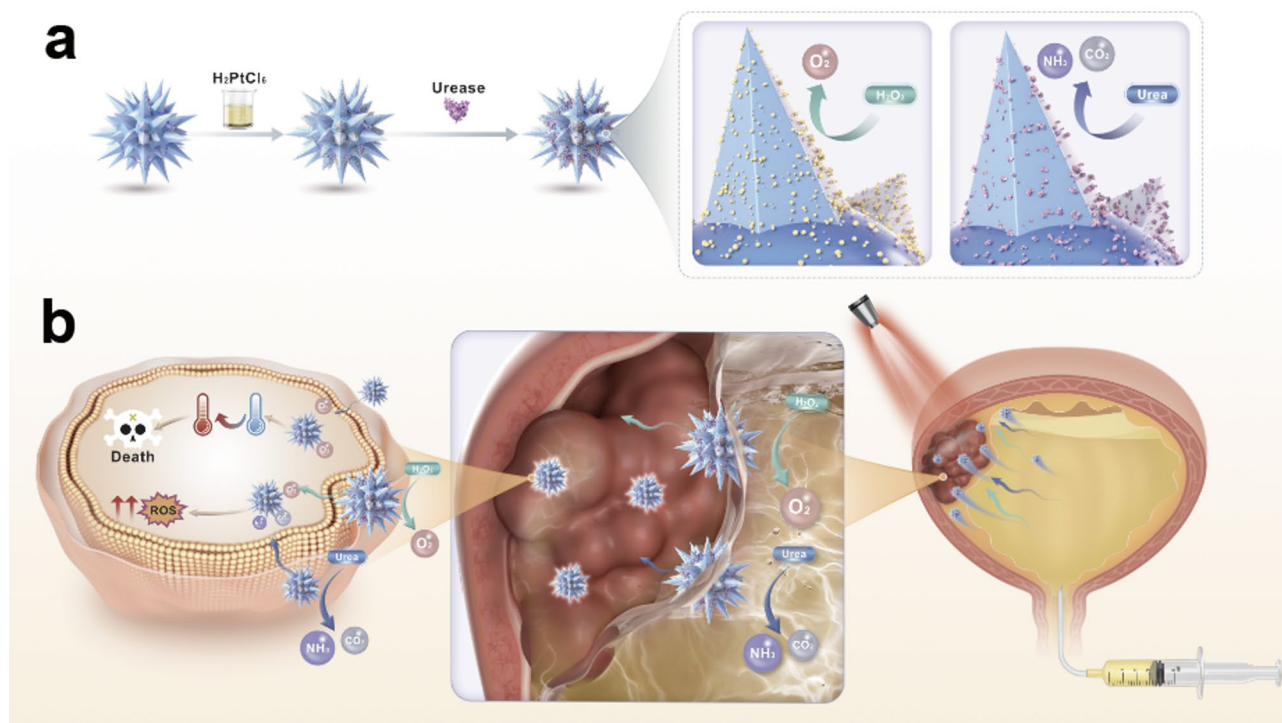


Fig. 1 Schematic illustration of the synthesis and tumor-inhibiting mechanism of Au-Pt@ur NPs. **(a)** The Synthesis of Au-Pt NPs: Briefly, the Au NP served as the core for the surface deposition of Pt atoms to form Au-Pt NPs. Ureases were then covalently immobilized onto Au-Pt NPs via HS-PEG₂₀₀₀-NH₂Cl linker. **(b)** The Tumor-inhibiting Mechanism of Au-Pt NPs: after intravesical administration, Au-Pt@ur NPs gained the power for self-propulsion via catalyzing urea in the bladder cavity and hydrogen peroxide in the tumor microenvironment, thus deeply penetrating the tumor. The NIR irradiation activated the photothermal effect of Au-Pt@ur NPs, together with the induction of significant reactive oxygen species (ROS), to ablate tumors

surface loading capacity, enhanced surface adsorption, improved transmembrane transport and superior photothermal conversion efficiency compared to spheroidal nanoparticles [17–20]. Consequently, the average diffusion coefficient of the sea urchin-like Au-Pt@ur NPs reaches $1.67 \pm 0.11 \mu\text{m}^2/\text{s}$ (3.2 mM of H₂O₂ + 500 mM urea, H + U) and approximately 2-fold more than that of single-source powered nanomotors, indicating its high mobility and maintain high catalytic activity even in high urea environments [21]. Under near-infrared (NIR) irradiation, the intravesical Au-Pt@ur NPs, stimulated by dual energy sources, penetrates deeply into the tumor base, effectively eradicating orthotopic bladder tumors in all cases [22]. The preclinical data in this study underscore the significant potential of Au-Pt@ur NPs for intravesical therapy of bladder cancer.

Results and discussion

Physicochemical properties of nanoparticles

Au-Pt@ur NPs were prepared as depicted in Fig. 1. Briefly, the Au NP was constructed via a previously reported method [23] and served as the core for the subsequent surface deposition of Pt atoms [24]. Ureases were then covalently immobilized onto Au-Pt NPs via an HS-PEG₂₀₀₀-NH₂Cl linker. Transmission

electron microscopy (TEM) analysis indicated that both Au-Pt NPs and Au-Pt@ur NPs exhibited a distinct sea urchin-like morphology, characterized by the presence of ultrasmall particles densely distributed on their spikes, which were absent in Au NPs. A mist corona uniformly surrounding the NPs only can be observed in Au-Pt@ur NPs (Fig. 2a, SI. Figure 1a). The lattice fringes of Au-Pt@ur NPs were analyzed using high-resolution transmission electron microscopy (HRTEM) images. The results revealed that the lattice spacing of the nanocore was 0.238 nm, corresponding to the Au (111) crystal plane, and that of the spheroidal particles attached to the nanocore surface was 0.213 nm, consistent with the Pt (111) crystal plane (SI. Figure 1b). Energy-dispersive X-ray (EDX) spectrum analysis further confirmed the incorporation of Pt element in Au-Pt NPs, with elemental weights of 23.79 wt% for Au, 1.42 wt% for Ag and 0.85 wt% for Pt (Fig. 2b, c) [25]. The Pt on the nanocore surface, as determined by inductively coupled plasma mass spectrometry (ICP-MS), was estimated to be $(113.4087 \pm 44.383) \mu\text{g/L}$, corresponding to 0.77% of the total mass. The absorbance peak of Au NPs in the UV-vis spectrum was recorded at 820 nm, while that of Au-Pt NPs shifted to 789 nm and maintain at 796 nm after coating with urease, indicating the successful and stable linkage

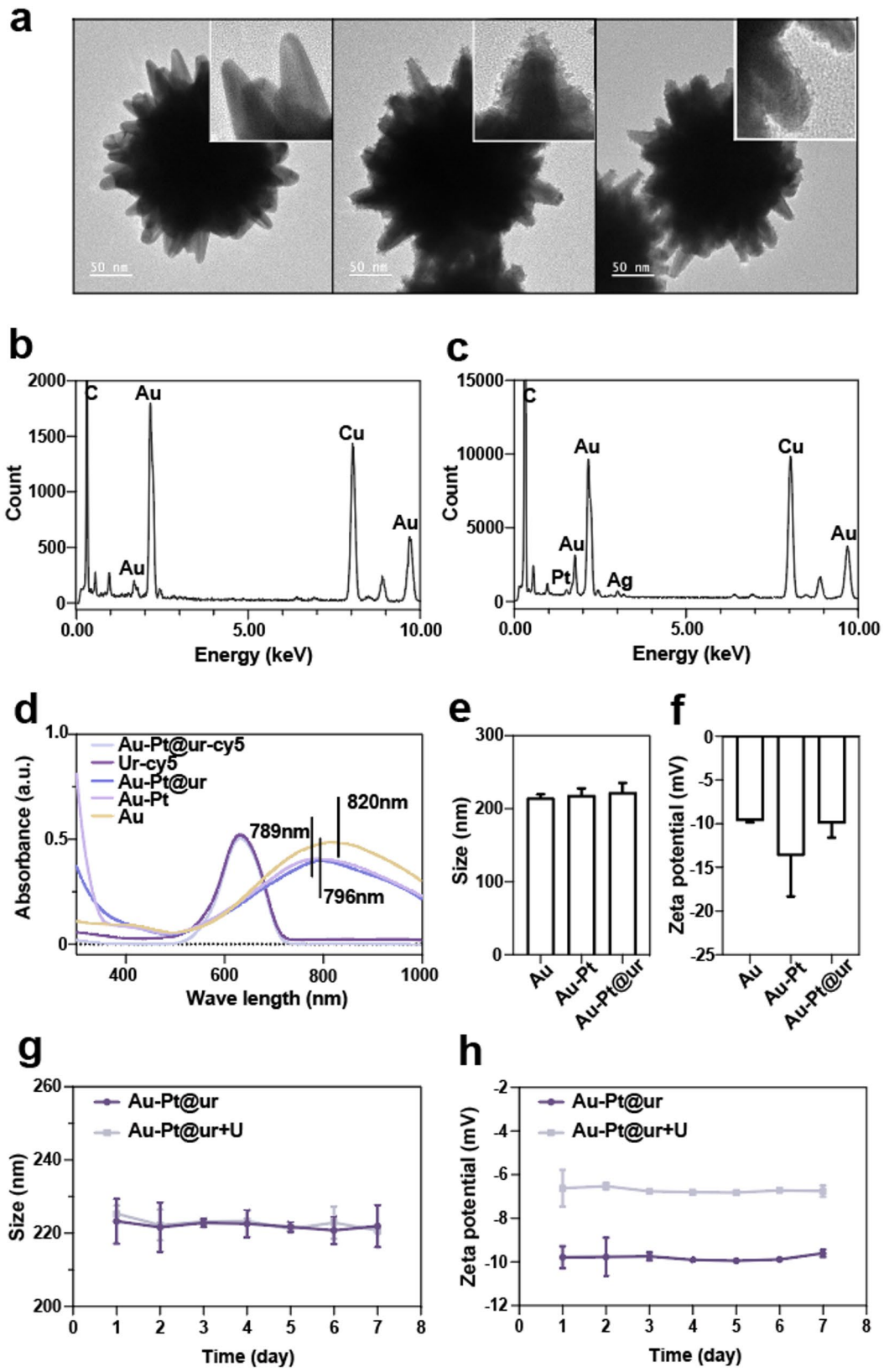


Fig. 2 (See legend on next page.)

(See figure on previous page.)

Fig. 2 Physicochemical characterization of Au-Pt@ur NPs. **(a)** TEM analysis depicting the morphological evolution from Au NP to Au-Pt@ur NP (From left to right: Au NP, Au-Pt NP, Au-Pt@ur NP). **(b)** EDX spectrum confirming the elemental composition of Au NPs. **(c)** EDX spectrum validating the presence of Pt in Au-Pt NPs. **(d)** UV-vis absorbance spectrum of Au NPs, Au-Pt NPs, Au-Pt@ur NPs, Ur-cy5 and Au-Pt@ur-cy5 NPs. **(e-f)** The average particle size and Zeta potential of Au NPs, Au-Pt NPs, Au-Pt@ur NPs. **(g)** The stability of Au-Pt@ur NPs in PBS (pH=7.4) and artificial urine, revealed by the size change. **(h)** The stability of Au-Pt@ur NPs in PBS (pH=7.4) and artificial urine, revealed by the Zeta potential change

of Pt to Au NPs. The absorbance peaks in the UV-vis spectrum of Au-Pt@ur-cy5 NPs partially overlapped with those of ur-cy5, proving that the successful conjugation of ureases to Au-Pt NPs (Fig. 2d). The average diameters of AuNPs, Au-Pt NPs, Au-Pt@ur NPs were 215 ± 3.6 nm, 218 ± 7.5 nm and 222 ± 10.4 nm, respectively (Fig. 2e, SI. Figure 1c), with their Zeta potentials being -9.67 ± 0.15 mV, -13.68 ± 3.79 mV and -9.96 ± 1.34 mV, respectively (Fig. 2f; Table 1). As shown in Fig. 2g-h, the average diameter and the Zeta potential of Au-Pt@ur NPs remained almost the same during seven days of incubation in PBS (pH=7.4) and artificial urine.

Catalytic properties and self-propulsion of Au-Pt@ur NPs

The catalytic efficiency of Au-Pt@ur NPs were compared with that of free urease or catalase, which can catalyze urea into ammonia and CO₂, or catalyze H₂O₂ into H₂O and O₂, respectively [26]. The catalytic bioactivity of the immobilized ureases in Au-Pt@ur NPs was minimally impaired, as compared to that of free ureases at an equivalent dose (Fig. 3a). The peroxidase-like activity of Au-Pt@ur NPs (2.2×10^8 Particles/ mL, 0.37 pM) was 1.48-fold greater than that of Au NPs and almost as strong as that of the catalase (0.05 μM) (Fig. 3b).

The motion of Au-Pt@ur NPs was dual-source powered via the conversion from chemical energy into kinetic forces. The trajectories of Au-Pt@ur NPs under different conditions were tracked using an optical tracking method (SI. Movie 1–2. Figure 3c). Under the urea concentration below 100 mM, Au-Pt@ur NPs exhibited Brownian motion, characterized by a linear increase of the mean-squared displacement (MSD). Once the urea concentration reached up to 100 mM, the increase of the MSD curve became non-linear, indicating the contribution of the self-propulsion (Fig. 3d). Moreover, the co-stimulation of H₂O₂ and urea (H+U) enhanced the self-propelled motion of Au-Pt@ur NPs compared to the stimulation of single fuel source. The effective diffusion coefficient (D_t) for each condition was determined by fitting the MSDs to the equation $MSD = 4D_t\Delta t$ [27]. Under unstimulated conditions, The D_t of Au-Pt@ur NPs was 0.026 ± 0.037 μm²/s, which was consistent with the theoretical Brownian diffusion constant (Stokes–Einstein equation), $D = kT/6\pi\eta r$, which calculates to 0.021 μm²/s. It became 5.3-fold, 9.5-fold, 9.56-fold, 23.4-fold, 35-fold

or 64.4-fold greater upon the exposure to 100 mM of urea, 300 mM of urea, 3.2 mM of H₂O₂, 300 mM of urea plus 3.2 mM of H₂O₂, 500 mM of urea or 500 mM of urea plus 3.2 mM of H₂O₂, respectively (Fig. 3e). Au-Pt@ur NP maintains stable self-propulsion even in high urea environments (100–500 mM), but the self-propelled effect weakened when the urea concentration reached up to 800–1000 mM (Fig. 3f-g), probably due to the inhibitory effect of ammonium ions produced by the urea hydrolysis on the catalytic activity of ureases [10]. Thus, Au-Pt@ur NPs can provide sufficient power for penetrating the urinary barrier, where the urea concentration can reach 300 mM [21].

The barrier-penetrating property of intravesical nanomotors

The urinary mucus serves as the first line of defense against intravesical drug penetration. In this study, porcine bladder mucus was employed to simulate this barrier in a Transwell diffusion assay (Fig. 4a). The dual source-powered group (Au-Pt@ur NPs H+U) translocated most rapid across the artificial mucus layer, with a transmucosal proportion of 47.4% after 1 h-incubation and 87.5% after 5 h-incubation. In contrast, only 5.32% or 7.53% of single-fuel-powered Au-Pt@ur NPs crossed the mucus after 5 h-incubation, which is approximately 2.67-fold and 3.78-fold greater than that of non-fuel powered Au-Pt@ur NPs (Fig. 4b).

The tumor-penetrating efficiency of Au-Pt@ur NPs was evaluated in different models. In 2D cell culture models, the transmembrane transport of dual-source powered Au-Pt@ur NPs was 1.59–6.03/1.30–52.41 folds greater than that of the control groups and dual-source powered nanoparticles in 253 J/T24 cells (Fig. 4c-f). Multicellular spheroids (MCSs) have been proposed as an in vitro 3D-cultured tumor model to mimic the solid tissue barriers presented in tumors against drug penetration [28]. Non-fuel powered Au-Pt@ur NPs failed to penetrate 253 J/T24 MCSs, as no fluorescence was detected either in the MCS border or in the inner region of the MCSs. Dual-fuel powered Au-Pt@ur NPs exhibited superior MCS-penetrating ability compared to non-fuel powered Au-Pt@ur NPs/single-fuel powered Au-Pt@ur NPs, with 14.75-fold/9.51-fold enhancement in the relative fluorescence intensity of NPs in the MCSs, and they were distributed throughout the MCSs after 12-hour penetration (Fig. 4g-h). The exposure of the MCSs to

Table 1 Size and zeta potential of NPs

	Au NPs			Au-Pt NPs			Au-Pt@ur NPs		
Size (nm)	215.9	210.5	219.4	211.6	215	229	217.9	212.9	237
PDI	0.244	0.240	0.229	0.256	0.228	0.242	0.235	0.268	0.290
Zeta	-9.52	-9.87	-9.63	-16.7	-16	-8.34	-11.8	-9.43	-8.65

both urea and H₂O₂ did not compromise their impermeability, as indicated by the lack of cell-impermeable Dextran (MW: 40 kD) distribution in the MCSs (SI. Figure 1d-e) [29].

The tumor-penetrating efficiency of intravesical Au-Pt@ur NPs was evaluated in orthotopic Bca models. Au-Pt@ur NPs were instilled intravesically and maintained for 2 h. As depicted in Fig. 5, no fluorescence derived from non-fuel powered Au-Pt@ur NPs was observed in the tumors, and they accumulated mainly in the bladder cavity. The tumor-penetrating depth of single-fuel powered Au-Pt@ur NPs was quite limited to the superficial layer. The dual-fuel powered Au-Pt@ur NPs demonstrated deep penetration and were almost uniformly distributed throughout the tumor tissue. Consequently, their fluorescence intensity of dual-fuel powered Au-Pt@ur NPs within the tumor tissue in the tumor tissue was significantly greater, being 14.88-fold/1.73-fold higher than that of non-fuel powered/single-fuel powered Au-Pt@ur NPs (SI. Figure 1f).

Cytotoxicity and photothermal efficiency of Au-Pt@ur NPs in vitro

The cytotoxicity of Au-Pt@ur NPs was assessed via CCK-8 cell viability assay kit. Both Au-Pt@ur NPs, Au-Pt NPs and Au NPs exhibited non-toxicity to various cell types when their particle concentration was lower than 0.37 pM (2.2×10^8 Particles/ mL). Once the particle concentration exceeded 1.11 pM or 0.74 pM, the cell viability of SVHUC-1 and T24 or 253 J was impaired, respectively (Fig. 6a-b, SI. Figure 1g). The additional presence of H₂O₂ (3.2 mM) or urea (300 mM) didn't change the toxicity profile of Au-Pt@ur NPs in all types of cells, whereas 808 nm laser irradiates (L) significantly enhanced the cytotoxicity of Au-Pt@ur NPs, leaving the viability dropped by 53.27% (Fig. 6c-e). Under the circumstance of L + H + U, 52.5% of cells underwent apoptosis (Fig. 6f-g) and 7-fold more ROS was generated, compared to the control group. Cells receiving the Au-Pt@ur NPs L + H/L + U were 16.24%/28.00% less apoptotic and generated 50% less ROS than those treated by L + H + U (Fig. 6h-i). Hypoxia-inducible factor (HIF) is a key transcription factor for hypoxic adaptation in BCa [30]. Western blot test showed that Au-Pt@ur NPs can stabilize the expression of HIF-1a (SI. Figure 1h). Dihydroethidium (DHE) fluorescence, indicative of the ROS levels in

bladder, in orthotopic BCa models receiving Au-Pt@ur + H or Au-Pt@ur + H + U groups was 1.97-folds or 1.80-folds stronger than that in the control, respectively (SI. Figure 2a-b). Furthermore, The results indicated that only Au-Pt@ur supplemented with both H₂O₂ and urea disrupted the tube formation by endothelial cells (HUVECs), while the effect became weaker once deprived of H₂O₂ or urea and even disappeared in the absent of Au-Pt@ur (SI. Figure 2c-e).

Photothermal efficiency of Au-Pt@ur NPs

Compared with spherical gold nanoparticles, sea urchin-like Au NPs displayed a much wider range of light adsorption, thus resulting in higher photothermal conversion efficiency [22]. Furthermore, the functionalization of Au nanoparticles with Pt leads to the enhanced longitudinal surface plasmon resonance (LSPR) bands, endowing them with superior photothermal efficacy for cancer therapy compared to their unmodified Au NP counterparts [31–32]. As shown in Fig. 7a, Au-Pt@ur NPs demonstrated remarkable stability at high temperature (67.5 °C) and after five heating-cooling actuation cycles. According to the heating-cooling actuation cycles, the photothermal conversion efficiency (PCE, η) was calculated to be 76.61% (Fig. 7b, SI. Figure 2f) and highly ranked compared to other types of nanoparticles (Table 2). The infrared thermal mapping was utilized to directly monitor the intravesical temperature change induced by Au-Pt@ur NPs under L + H + U (Fig. 7b). The results showed a significant temperature increase in the luminal environment, reaching up to 64.4 °C after 10 min of NIR irradiation, which is well above the temperature threshold (40–44 °C) that tumors cannot tolerate [30]. However, the increase of temperature (11 °C) in the bladder lumen filled with PBS buffer was mild (Fig. 7c).

The photothermal effect of intravesical Au-Pt@ur NPs to tackle BCa was evaluated in murine orthotopic BCa models. The IT followed a standard protocol recommended by previous studies [40]. IT was repeated totally five times at 5-day intervals; the growth of orthotopic BCa was monitored using the bioluminescence imaging with luciferase-luciferin pairs every 5 days, and the body weight of each case was monitored every 5 days. The NIR irradiation was applied 2 h post intravesical instillation, with its focus on the lower abdomen, power density of 1.5 W·cm⁻², and exposure time of 600 s [29]. In vivo bioluminescence imaging

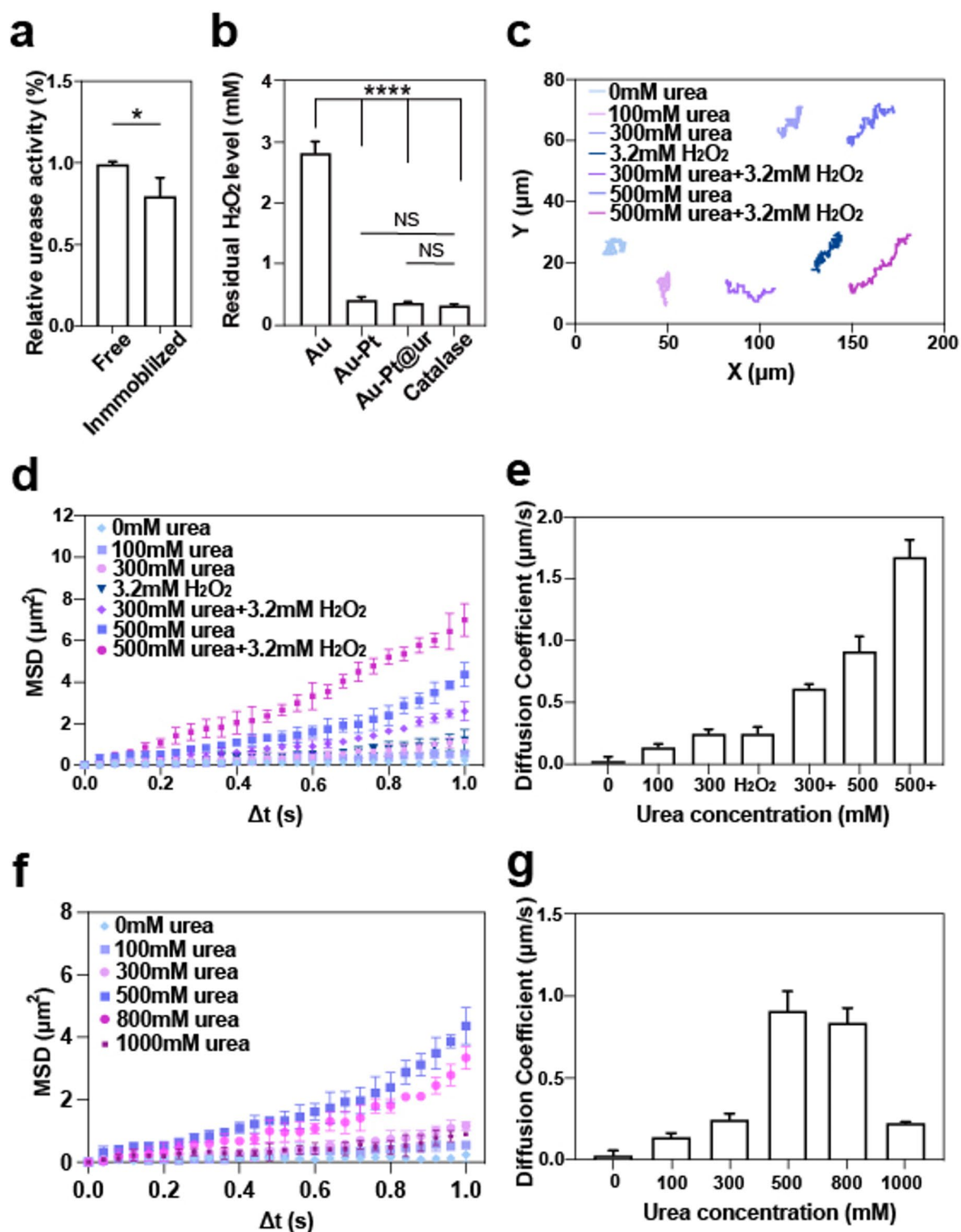


Fig. 3 Catalytic efficiency and self-propulsion of Au-Pt@ur NPs. **(a)** Comparative analysis of the catalytic activity of free urease and urease immobilized on Au-Pt@ur NPs. **(b)** Comparative analysis of the catalase-like activity of different NPs, indicated by the residual H₂O₂ after 20-min catalyzation. **(c)** Representative 20-second tracking trajectories of Au-Pt@ur NPs under different stimulations. **(d)** Average MSD versus time interval (Δt) analyzed from tracking trajectories, showing MSD curves of individual Au-Pt@ur NPs at varying urea concentrations and with or without 3.2 mM H₂O₂. **(e)** Diffusion coefficient values extracted from the linear regression of average MSD plots (for panels c-d, 30 nanoparticles were analyzed, and the error bars in panel e represent the standard error of mean, $N=30$). **(f)** MSD curves of Au-Pt@ur NP at different urea concentrations. **(g)** Diffusion coefficient values extracted from the linear regression of average MSD plots (for panels f, 30 nanoparticles were analyzed, and the error bars in panel g represent the standard error of mean, $N=30$)

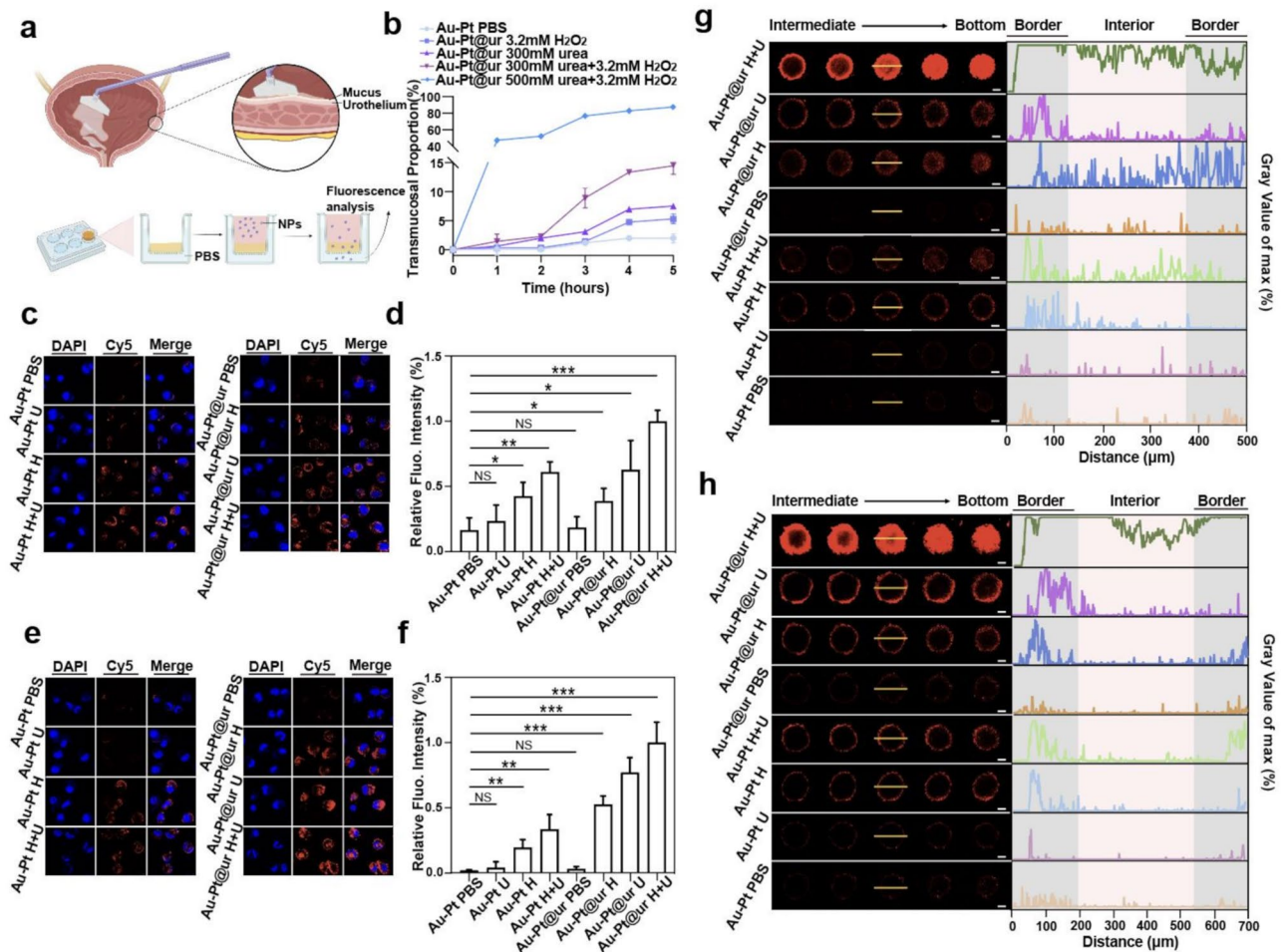


Fig. 4 The barrier-penetrating property of intravesical nanomotors. **(a)** Schematic diagram of the Transwell diffusion assay. **(b)** Quantification of the transmucosal proportion of Au-Pt@ur-cy5 NPs after a timed diffusion at 37 °C; a porcine mucus layer with the thickness of 20 μm was seeded onto a Transwell polycarbonate membrane in a pore size of 0.4 μm, and 100 μL of NPs + solvent was afterward loaded onto the upper Transwell chamber with 1000 μL of PBS buffer (pH = 7.4) in the lower chamber; NPs in the lower chamber was deemed as the transmucosal portion. **(c)** Tumor penetration of Au-Pt-cy5 NPs and Au-Pt@ur-cy5 NPs in 253 J cells, imaged by a confocal microscope from Cy5/DAPI-fluorescence channels; NPs 12 h-incubation. Scale bar: 100 μm. **(d)** Relative Cy5-fluorescence intensity of the corresponding 253 J cells in panel (c). **(e)** Tumor penetration of Au-Pt-cy5 NPs and Au-Pt@ur-cy5 NPs in T24 cells, imaged by a confocal microscope from Cy5/DAPI-fluorescence channels; NPs 12 h-incubation. Scale bar: 100 μm. **(f)** Relative Cy5-fluorescence intensity of the corresponding T24 cells in panel (e). **(g-h)** Tumor penetration of Au-Pt-cy5 NPs and Au-Pt@ur-cy5 NPs in 253 J/T24 multicellular spheroids, imaged by a confocal microscope from Cy5-fluorescence channel; Z-stack covered the course from the intermediate layer to the bottom layer at 20 μm intervals; NPs 12 h-incubation. Scale bar = 100 μm

analysis revealed that the tumor growth regressed rapidly at the initial phase of IT of Au-Pt@ur NPs plus L + H + U (**Figur 7d**), following a second IT tumors in nearly all cases got chemo-resected and no recurrence was observed in the 3-week follow-up (**SI. Figure 3a-b**). Urea or H₂O₂ deprivation greatly impaired its anti-cancer ability, indicated by a slight decrease in the tumor volume, although tumor eradication in 100% of mice was completed finally. And the lack of urea and H₂O₂ supply eliminated the anti-tumor activity of intravesical Au-Pt@ur NPs, even under the NIR

irradiation (**Fig. 7e**). The self-propelled tumor-penetration is therefore a prerequisite for effective photothermal IT. The weight gain and weigh loss were detected in the mice with reduced tumor burden and tumor progression, respectively (**Fig. 7f-g**). Histopathological examination proved the photothermal IT via Au-Pt@ur NPs induced no side effect to of normal organs, including the heart, liver, spleen, lung and kidney (**Fig. 7h**). The blood test, indicative of the liver and kidney function, further demonstrated the biosafety of the photothermal IT via Au-Pt@ur NPs (**SI. Figure 3c-f**).

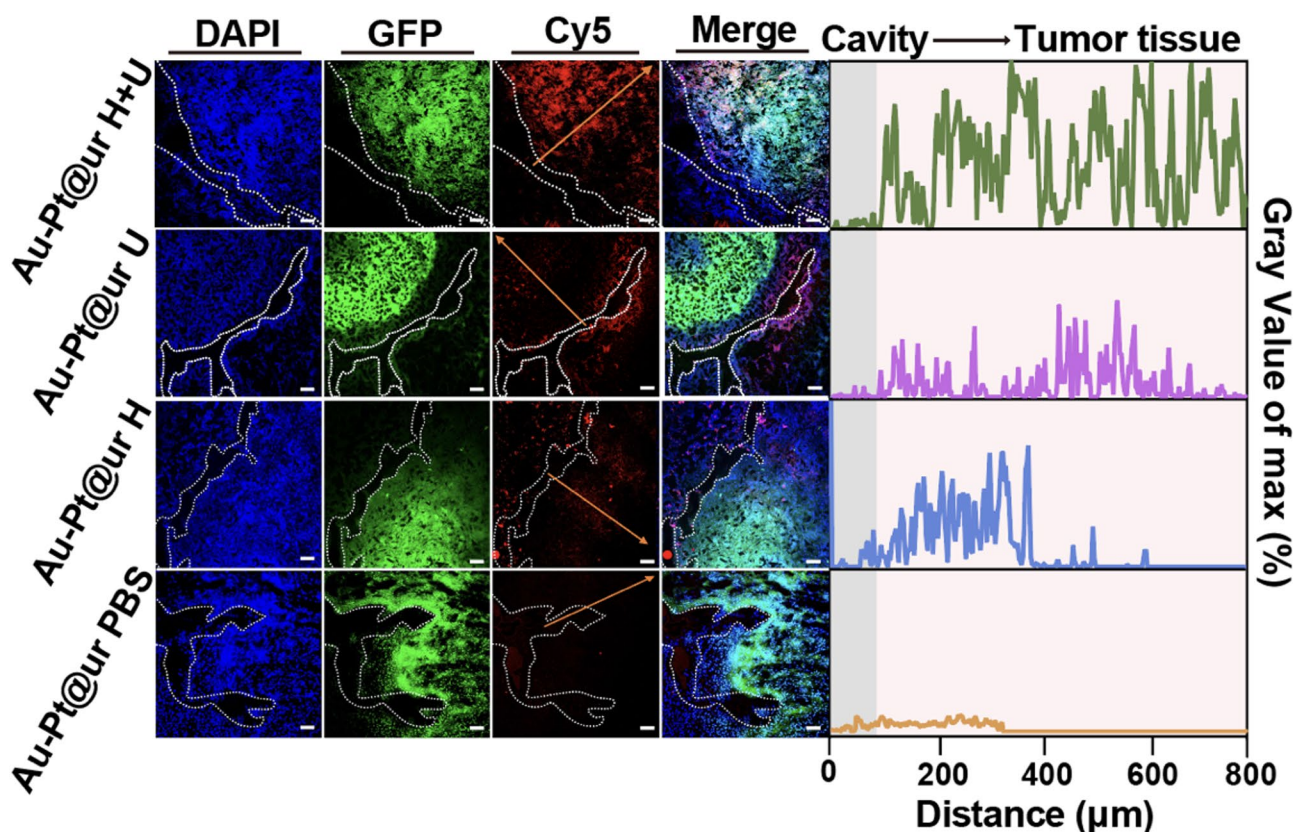


Fig. 5 Tumor penetration of Au-Pt@ur NPs in orthotopic BCa models (GFP-transfected T24 cells). After 2 h-intravesical instillation, the bladders were frozen and sectioned (20 μm thick) in a cryostat and the sections were imaged by a confocal microscope from DAPI (nuclei), eGFP (Bca cells), and Cy5 (NPs) channels. Scale bar: 100 μm

Conclusions

In summary, we have developed a dual-source powered sea urchin-like nanomotor, featuring a core of gold nanoparticles adorned with ultrasmall platinum nanoparticles and ureases on its surface. They gained the capabilities of high tissue-penetration, low toxicity, and efficient photothermal therapy both in vitro and in vivo, and displayed the concentration-dependent enhanced non-linear diffusion in an H_2O_2 and urea solution, highlighting their self-propelled motion via chemical energy conversion. And therefore, the bladder lumen and the tumor microenvironment provide dual-source fuels to support the tumor-penetration of Au-Pt@ur NPs. Remarkably, dual-source powered Au-Pt@ur NPs could penetrate deep inside the bladder and effectively suppressed tumor growth through photothermal therapy. The preclinical data in this study underscore the significant potential of Au-Pt@ur NPs for intravesical therapy of bladder cancer. However, the clinical translation of our nanomotors face three dilemmas. The safety and biocompatibility of our nanomotors, as a major concern, need further in vivo investigation. And their potential for tackling other types of malignancy is limited due to a scarce

distribution of urea owned by other tumors and weak single source-powered propulsion. Though safe and effective, the large-scale production, good quality control and stable long-term storage of our nanomotors are critical prerequisite for commercial use.

Experimental section

Materials

Au nanoparticles (Au NPs) were constructed via a previously reported method [23], briefly, 10 mL of $\text{HAuCl}_4 \cdot 3\text{H}_2\text{O}$ (16961-25-4, 99%, Sigma-Aldrich) aqueous solution (10 mM) was added to 10 mL of water in a 25 mL beaker with a strong magnetic stirring. Then, 7.5 mg/ml AA powder was rapidly added to the water solution and allowed to react for 5 min. Hexadecyltrimethylammonium bromide (CTAB, 57-09-0, 99%) was purchased from Sigma-Aldrich (Shanghai, China). Silver nitrate (AgNO_3 , 7761-88-8, 99%) was purchased from Aladdin (Shanghai, China). Ascorbic acid (AA, 50-81-7, 99%) was purchased from Sigma-Aldrich (Shanghai, China). Hydrogen hexachloroplatinate hexahydrate (H_2PtCl_6 , 26023-84-7, 99.9%) was purchased from Sigma-Aldrich (Shanghai, China). 200–300 U urease (9002-13-5, 98%) was purchased

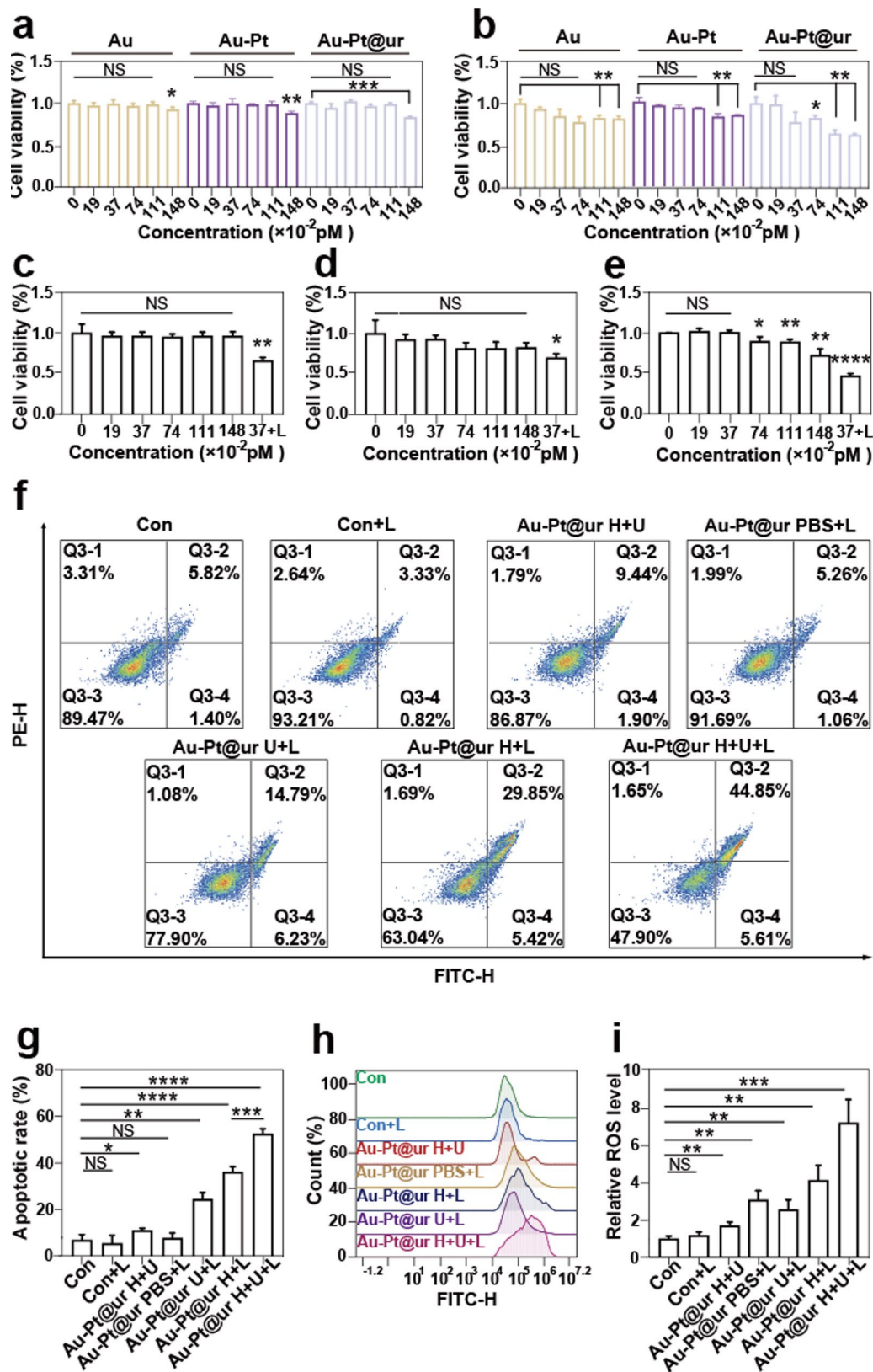


Fig. 6 (See legend on next page.)

(See figure on previous page.)

Fig. 6 In vitro anti-cancer activity of Au-Pt@ur NPs. **(a-b)** Concentration-dependent cytotoxicity of Au NPs or Au-Pt@ur NPs on T24 cells or 253 J cells for 12 h-incubation, illustrated by the CCK-8 assay. **(c-e)** Concentration-dependent cytotoxicity of Au-Pt@ur NPs + U (+L), Au-Pt@ur NPs + H (+L), Au-Pt@ur NPs + H + U (+L) in T24 cells for 12 h-incubation, illustrated by the CCK-8 assay. **(f)** Cell apoptosis effect, illustrated by the flow cytometry analysis from the Annexin V-FITC-fluorescence channel and PI-fluorescence channel. **(g)** Averaged apoptotic rate of T24 cells for 12 h-incubation, illustrated by the flow cytometry analysis assay. **(h)** Intracellular ROS generation, illustrated by the flow cytometry analysis from the Annexin V-FITC-fluorescence channel. **(i)** Relative ROS level of T24 cells for 12 h-incubation

from Macklin (Shanghai, China). Sulfo-Cy5 NHS ester (sulfo-NHS-Cy5, 2230212-27-6, 95%) was purchased from Aladdin (Shanghai, China). HS-PEG₂₀₀₀-NH₂HCL (Q-0146715, 95%) was purchased from JenKem Technology (Beijing, China). Acetyloximic acid (AHA, A106239, 98%) was purchased from Aladdin (Shanghai, China). H₂O₂ quantification assay kit was purchased from Sangon Biotech (BC3595, Shanghai, China). Urease activity detection kit was purchased from Solarbio (BC4115, Beijing, China). DMEM (high glucose), penicillin–streptomycin, trypsin-EDTA, fetal bovine serum (FBS), and phosphate-buffered saline (PBS, pH 7.4) were obtained from Thermo Fisher Scientific (Waltham, MA, USA). The Cell Count Kit-8 (CCK8 kit) was purchased from LABLEAD (CK001, Beijing, China). Methylcellulose (9004-67-5), Annexin V-FITC Apoptosis Detection Kit (C1062), Reactive Oxygen Species Assay Kit (S0033) and Hoechst 33,342 (C1026, 1000×) were purchased from Beyotime Biotechnology Co., Ltd. Matrigel was purchased from Corning (354248, New York, America).

The size, shape and HRTEM of nanoparticles were observed using TEM (JEM-F200, JEOL, Japan). ICP-MS was tested using Agilent 7800 (America). The UV–Vis–NIR absorption spectra of the nanoparticles were tested using a spectrophotometer (Thermo Fisher). The size distribution and Zeta potential of nanoparticles were evaluated by a Zetasizer nano ZS particle analyzer (Malvern Instruments Co., Ltd.). The movement of Au-Pt@ur NPs was recorded by Particle Metrix (ZetaView). Fluorescence analysis of mucus penetration and cytotoxicity were evaluated by a Multi-Mode Microplate Reader (Synergy Mx, Bio-Tek Instruments Inc., Winooski, US). Fluorescence images were detected using CLSM (confocal laser scanning microscope, Leica DMI8). Flow cytometer analysis were tested by BD Biosciences (New Jersey, US). The bioluminescence of BCa was monitored by IVIS Lumina XRMS Series III (PerkinElmer Inc., Waltham, US) HE stained tissues were imaged by an inverted microscope (TS 100, Nikon Ti, Japan). The thermal maps were provided by a thermal imager (FLIR).

Synthesis of Au-Pt nanoparticles

The synthesis of Pt-modified Au NPs were silver ions-assisted [41–42]. 200 µl Au NPs (~50 pM), 500ul 200 mM CTAB, 10 ul 2 mM AgNO₃ were added together

and diluted with sterile double distilled Water (dd water) to a 5 ml reaction system. The reaction mixture was heated to 50 °C in a dd water bath and stirred for 200 rpm 10 min before adding 40 ul 100 mM AA. Continuously stirring for 1 h then add 60 ul 10 mM H₂PtCl₆ and react for another 1 h. Afterward, microparticles were removed by centrifugation at a rotating speed of 3000 rpm for 10 min and wash twice with dd water to obtain the preliminary product Au-Pt NPs. Au-Pt NPs exhibit strong solubility in dd water and can be stored under 4 °C.

Synthesis of Au-Pt@ur nanoparticles

2 ml of pre-synthesized Au-Pt NPs was mixed with 6.25×10^{-5} mM HS-PEG₂₀₀₀-NH₂HCL and stirred at low speed (100 rpm) for 12 h, then 4×10^{-3} µM urease was added and reacted for another 12 h. To remove excess impurities and unreacted reagents, the Au-Pt@ur NPs were centrifuged using an ultrafiltration centrifuge tube (MW: 30KD, Millipore) under 3000 rpm 15 min. This centrifugation step was repeated twice to ensure thorough purification and gain the final product Au-Pt@ur NPs (~4.625 pM). 16.6 mM sulfo-Cy5 NHS ester can be added for 30 min to get Au-Pt@ur-cy5 NPs, and addition of 0.5 mM AHA can effectively inhibit the activity of urease to obtain the Au-Pt-cy5 NPs, the appeal ultrafiltration method also available here. All the resulting products should be stored at 4 °C until use.

Pt activity assay

The catalytic activity of Pt immobilized on Au-Pt@ur NPs was assessed indirectly by monitoring the consumption of H₂O₂. Au-Pt@ur NPs was reacted with 3.2 mM H₂O₂ [8]. For 20 min and the concentration of hydrogen peroxide left from the reaction was detected using a H₂O₂ quantification assay kit.

Urease activity assay

The enzymatic activity of urease immobilized on Au-Pt@ur NPs was evaluated with urease activity detection kit from Solarbio. The production of 1 µg of NH₃-N per mg of protein per min is defined as an enzyme activity unit. The enzymatic activity of urease we purchased and adopted is found to be 200–300 U/mg.

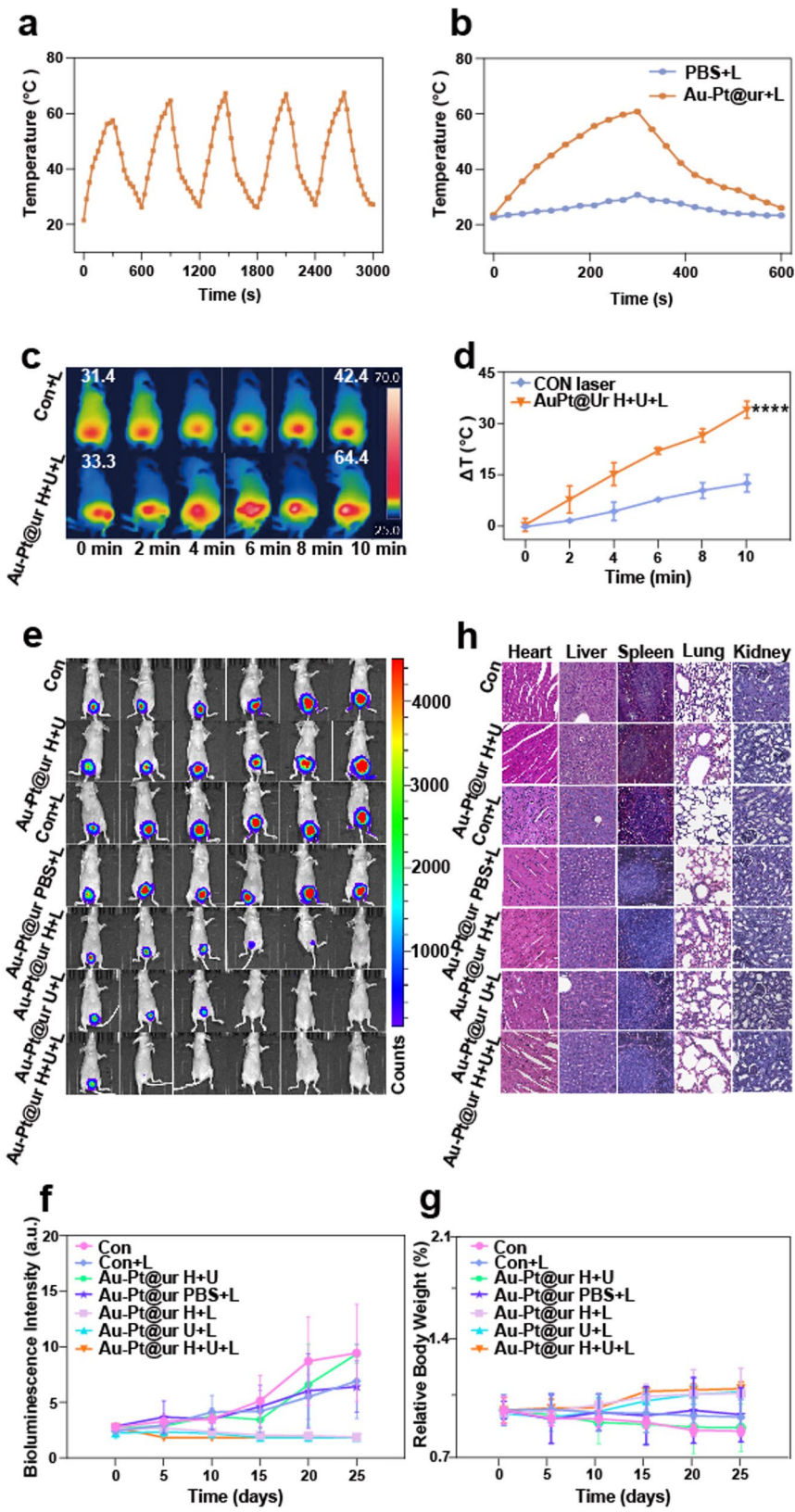


Fig. 7 (See legend on next page.)

(See figure on previous page.)

Fig. 7 (a) Temperature change of Au-Pt@ur NPs after 5 cycles (on/off) irradiation by 808-nm laser ($1.5 \text{ W}\cdot\text{cm}^{-2}$). (b) Heating/cooling curves for Au-Pt@ur NPs and PBS (808-nm laser, $1.5 \text{ W}\cdot\text{cm}^{-2}$). (c-d) Infrared thermal mapping images, and corresponding temperature profiles of tumor regions after irradiated with an 808-nm laser ($1.5 \text{ W}\cdot\text{cm}^{-2}$) for different times (0~10 min) at 2 h-intravesical instillation of Au-Pt@ur NPs or PBS. (e) Anticancer efficacy of different intravesical therapies, illustrated by bioluminescence imaging with luciferase-luciferin pairs. (f) In vivo bioluminescence intensity curves of orthotopic BCa in the corresponding groups in panel (e). (g) Averaged body weight of mice in the corresponding groups in panel (e). (h) Histopathological analysis of the representative bladders after the completion of intravesical therapies from the corresponding mice in panel (e) by H&E staining, scar bar: 100 μm

Optical video recording

Particle Metrix was utilized to observe and record the movement of Au-Pt@ur NPs. 80 μL Au-Pt@ur NPs solution (4.625 pM) was added into 990 μL of urea solution in different concentration (0, 100, 300, 500 mM), with or without 3.2 mM H_2O_2 . The mixture thoroughly homogenized to ensure uniform distribution of the Au-Pt@ur NPs within the solution. The videos of the movement of nanoparticles were recorded for up to 20 s via at the frame rate of about 25 fps.

Mean-square-displacement analysis

The movement videos of Au-Pt@ur NPs in different concentration of solution were analyzed using a self-developed program based on Python to extract their movement trajectories. Thereafter, MSD was calculated using the following formula: $\text{MSD}(\Delta t) = [(x_i(t + \Delta t) - x_i(t))^2]$ ($I=2$, for two dimensional analysis). Subsequently, the following formula was applied to obtain the diffusion coefficient (D), $\text{MSD}(\Delta t) = 4D\Delta t$, which works for small particles with low rotational diffusion for small time intervals. More than 30 particles were analyzed to obtain statistics in each experimental group.

Mucus-penetration assay

The mucus layer was gently scraped off and placed in a centrifuge tube at 1000 g, centrifuged for 30 min, centrifuged twice, then the supernatant was extracted and sterilized under UV for 30 min. Sterilized mucus layer were seeded onto a polyester membrane filter of a Transwell chamber (0.4 μm pore size) with the thickness of about 20 μm , and place in incubator overnight. After that, 80 μL 4.625pM Au-Pt@ur-cy5 NPs + 20 μL solvent were mixed well in 1 ml no FBS DMEM and added 100 μL onto the topside of each mucus layer, respectively, with 1 mL of PBS filling the lower chamber. During 0–5 h, we collected 100 μL of PBS buffer containing the leakage from the upper chamber for fluorescence analysis via a Multi-Mode Microplate Reader per hour.

Cell culture

bCa cells (T24 and 253 J) and normal urothelium cells (SVHUC-1) were cultured in DMEM. HUVECs were cultured in F12K. All cell lines were supplemented with 10% fetal bovine serum and 100 U/mL 1%

penicillin/streptomycin and maintained at 37 °C. T24, 253 J, SVHUC-1 and HUVECs cells were obtained from the National Collection of Authenticated Cell Cultures, China.

Penetration efficiency in 2D cell culture models and MCSs

T24 or 253 J cells were suspended in DMEM (containing 0.12% w/v methylcellulose), seeded into 8 laser confocal Petri dishes (10^5 cells per microplate) and incubated for 12 h. Then, medium of each dish was discarded and washed 3 times with PBS before administration. Each group was administered according to 80 μL nanoparticles + 20 μL solvent, mixed with serum-free DMEM presented as 1 ml system, namely, Au-Pt-cy5 + PBS, Au-Pt-cy5 + U, Au-Pt-cy5 + H, Au-Pt-cy5 + H + U, Au-Pt@ur-cy5 + PBS, Au-Pt@ur-cy5 + U, Au-Pt@ur-cy5 + H, Au-Pt@ur-cy5 + H + U. As for the preparation of MCSs, $5 \times 10^6/\text{ml}$ T24 cells or $8 \times 10^6/\text{ml}$ 253 J cells were suspended in DMEM (containing 0.12% w/v methylcellulose) and mixed evenly. Then, 20 μL of the cell suspension was dropped on the lid of the cell culture plate to form uniform droplets and 10 ml PBS was added to the plate for keeping the droplets moist. After being placed in a 37 °C incubator for 60 h, dense spheroids were transferred to a low adhesion 24-well plate and equally divided into 8 groups with the same appeal to administration. After 12 h, fluorescence imaging was performed under CLSM after three gentle rinses with PBS and ImageJ software was used for analysis.

Penetration efficiency in murine orthotopic bCa models

All animal procedures were approved by the Laboratory Animal Management Committee at Zhejiang Provincial People's Hospital (No. 20240614132209126857). All animal procedures were performed according to the guidelines of the Administration Committee of Experimental Animals in Zhejiang Province and the Ethics Committee of Zhejiang Provincial People's Hospital. Six- to eight-week-old nu/nu female mice were anesthetized by inhalation of 1% isoflurane in an oxygen gas mixture and kept on a heated platform during catheterization procedures. Lubricated angiocatheters were inserted into the urethra. After full insertion, the bladder was flushed with 80 μL of sterile PBS and pretreated with 80 μL of poly-L-lysine for 15 min. A single-cell suspension of 5×10^5 GFP-transfected T24 cells in

Table 2 Comparative analysis of photothermal conversion efficiency among different nanomaterials

Nanoparticles	Irradiation	PCE (%)	Ref.
2D niobium carbide (Nb ₂ C) nanosheets	808 nm	34.9%	[33]
	1064 nm	46.65%	
As semiconducting polymer nanoparticles (As SPs)	808 nm	~71%	[34]
Thiophene-benzene-diketopyrrolopyrrole (TBD)-based polymer nanoparticles	808 nm	68.1%	[35]
Au plasmonic blackbodies	1064 nm	80.8%	[36]
	808 nm	88.6%	
Au nanomatryoshkas	808 nm	63%	[37]
Au nanoshells	808 nm	39%	[37]
Polymer NP@ FeIII/tannic acid shell	498 nm	40%	[38]
Electron donor-acceptor conjugated semiconducting polymer nanoparticles	635 nm	62.3%	[39]

100 μ l of PBS was inoculated into the bladder and preserved for 1 h. During the entire procedure, the mice were kept under anesthesia for 2 h before the catheter was gently removed from the urethra. The mice were monitored every day for any signs of pain and distress. After 1 week, the nu/nu female mice bearing bCa were anesthetized by inhalation of 1–2% isoflurane in an oxygen gas mixture and kept on a heated platform during catheterization procedures. Lubricated angiocatheters were inserted into the urethra. After full insertion, the bladder was flushed with 80 μ l of sterile PBS. 80 μ l Au-Pt@ur NPs were mixed with 20 μ l different solutions to form 4 groups (PBS, H₂O₂, urea, H₂O₂ + urea), and were intravesically instilled and preserved for 2 h, respectively. The bladder was washed twice with PBS. The mice were sacrificed immediately. The tissues (including the bladder, heart, liver, spleen, lung and kidney) were harvested for further histopathological examination by HE staining. The bladders were frozen and sectioned (20 μ m thick) in a cryostat and the sections were examined by using CLSM.

Cytotoxicity assay

T24, 253 J, and SVHUC-1 were seeded in 96-well plates with 8,000 cells per well for tumor cells and 12,000 per well for SVHUC-1. 200 μ l of DMEM (with 10% serum) was added and placed in an incubator for 24 h. Configure different concentrations of nanomaterials separately, we selected the interval of 0.5–4 times after testing, for example, 80 μ l of Au-Pt@ur NPs and 20 μ l of urea + H₂O₂ were prepared into 1 ml with serum-free DMEM and added 100 μ l to each well. After administration for 12 h, the cell viability was measured with CCK-8 cell viability assay kit. And the cell viability was measured in the same way after administration and radiated for 600 s under 1.5 W·cm⁻².

Flow cytometry analysis

Generally, T24 cells were seeded into 24-well plates at a density of 1×10^5 cells per well and incubated for 12 h. 80 μ l of Au-Pt@ur NPs and 20 μ l of solvent (H₂O₂, urea, H₂O₂ + urea) were administrated for another 12 h, and we irradiated the cells with a laser power density of 1.5 W·cm⁻². Afterward, stained with Annexin V-FITC/PI at room temperature for 15 min washed twice with PBS buffer (pH 7.4) and digested with trypsin. Detached cells were collected using centrifugation at 300 g for 3 min to remove trypsin and washed with PBS buffer (pH = 7.4). The cells were resuspended in PBS buffer (pH 7.4) and transferred to a flow cytometer (BD Biosciences, New Jersey, US). The average fluorescence intensity was determined by counting every 5000 cells. The experiment was independently repeated three times, and the data were analyzed using FlowJo software. The results are presented as the mean \pm the standard deviation (S.D.). Detection of intracellular ROS generation is in the same way, just replaced the fluorescent-labeled materials with DCFH-DA and incubated at 37 °C for 20 min.

In vitro angiogenesis characterization

To detect the formation of tubes, 200 μ l of HUVECs were seeded into 48-well plate at a concentration of 3×10^4 cells/mL with material of each group. The plate was Preplanking with 4°C Matrigel. Then the plate was incubated in 36°C for 6 h, HUVECs were photographed by microscope to count the number of tubes.

Photothermal therapy of Au-Pt@ur NPs treated bCa models

The nu/nu female mice bearing bCa originating from luciferase-transfected T24 cells were obtained by the same method as appeals. They were anesthetized by inhalation of 1–2% isoflurane in an oxygen gas mixture and kept on a heated platform during catheterization procedures. Lubricated angiocatheters were inserted into the urethra. After full insertion, the bladder was flushed with 80 μ l of sterile PBS. 80 μ l Au-Pt@ur NPs were mixed with 20 μ l different solutions to form 4 groups (PBS, H₂O₂, urea, H₂O₂ + urea), and were intravesically instilled and preserved for 2 h, respectively. Saline was also intravesically instilled as in the control group. After each administration, irradiated the lower abdomen with a laser power density of 1.5 W·cm⁻² with irradiation time of 600 s. Intravesical instillation and photothermal therapy were performed every five days for a total of five times. The mice were intraperitoneally injected with 100 mg/kg D-luciferin to monitor the in vivo bioluminescence of tumors using the IVIS Spectrum system with an excitation wavelength of 640 nm and an emission wavelength of 660 nm

every 5 d. The thermal maps were provided by a thermal imager (FLIR). For the case whose orthotopic bCa got chemo-resected within five rounds of intravesical therapy, the duration of observation on its tumor growth and the change body weight was extended to another 3 weeks. Finally, all murine were sacrificed, and tissues (including bladder, heart, liver, spleen, lung, and kidney) were harvested for further histopathological examination by HE staining. The tissues were imaged using an inverted microscope. 5 groups (Control, Au-Pt@ur PBS, Au-Pt@ur + U, Au-Pt@ur + H, Au-Pt@ur + H + U) intravesically instilled and preserved for 2 h, respectively. All murine were sacrificed, and bladders were harvested for further histopathological examination by DHE staining and imaged by microscope.

Statistical analysis

The testing values of repeated measurements were averaged to obtain the data of general analysis experiments, and relevant data are expressed as mean \pm SD. The statistical analysis was performed using GraphPad Prism software (ver 9.5.0). Statistical significances were examined by t test with $^*P < 0.05$.

Supplementary Information

The online version contains supplementary material available at <https://doi.org/10.1186/s12951-025-03446-3>.

Supplementary Material 1: Movie S1 1: Optical video recording of Au-Pt@ur NPs in PBS via Particle Metrix

Supplementary Material 2: Movie S1 2: Optical video recording of Au-Pt@ur NPs in 3.2 mM H₂O₂ + 500 mM urea via Particle Metrix

Supplementary Material 3

Acknowledgements

Not applicable.

Author contributions

Yixuan Mou, Zhenghong Liu and Wentao Xu contributed equally. Yixuan Mou designed and implemented this research; Zhenghong Liu and Wentao Xu performed Au-Pt@ur characterization and analysis. Bin Zheng, Minghai Ma and Xiaowen Qin designed and performed the Au-Pt NP synthesis. Jiajia Zheng, Ran Ni and Haichang Li tested and analyzed the motion of Au-Pt@ur NP. Lei Wang, Yuchen Bai and Jinhai Fan, Xiaolong Qi assisted in the construction of orthotopic BCa models and tested photothermal therapy efficiency. Qi Zhang, Pu Zhang and Dahong Zhang provided financial support and supervised the project. The manuscript was written through contributions of all authors.

Funding

This work was supported by the National Natural Science Foundation of China (82300868 and 82473503).

Data availability

Data is provided within the manuscript or supplementary information files.

Declarations

Ethics approval and consent to participate

All animal procedures were approved by the Laboratory Animal Management Committee at Zhejiang Provincial People's Hospital (20240614132209126857). All animal procedures were conducted in accordance with the guidelines of the Administration Committee of Experimental Animals in Zhejiang Province and the Ethics Committee of Zhejiang Provincial People's Hospital.

Consent for publication

We give our consent for the manuscript to be published in *Journal of Nanobiotechnology*.

Competing interests

The authors declare no competing interests.

Author details

¹Urology & Nephrology Center, Department of Urology, Affiliated People's Hospital, Zhejiang Provincial People's Hospital, Hangzhou Medical College, Hangzhou 310014, Zhejiang, China

²Cancer Center, Department of Interventional Medicine, Zhejiang Provincial People's Hospital (Affiliated People's Hospital), Hangzhou Medical College, Hangzhou 310014, People's Republic of China

³Department of Urology, The First Affiliated Hospital of Jinan University, Guangzhou 510630, Guangdong, China

⁴Department of Urology, The First Affiliated Hospital, Xi'an Jiaotong University, Xi'an 710061, China

⁵Department of Nutrition and Food Hygiene, The National Key Discipline, School of Public Health, Harbin Medical University, Harbin 150081, P.R. China

⁶General Surgery, Cancer Center, Department of Hepatobiliary & Pancreatic Surgery and Minimally Invasive Surgery, Zhejiang Provincial People's Hospital (Affiliated People's Hospital), Hangzhou Medical College, Hangzhou 310000, Zhejiang, China

⁷Department of Thoracic Surgery, Tangdu Hospital, Air Force Medical University, Xi'an 710038, China

Received: 22 December 2024 / Accepted: 5 May 2025

Published online: 17 May 2025

References

- Nason GJ, Ajib K, Tan GH, Kulkarni GS. Bladder-sparing treatment options in localized muscle-invasive bladder cancer. *Expert Rev Anticancer Ther*. 2020;20(3):179–88. Epub 2020 Mar 9.
- Chade DC, Shariat SF, Dalbagni G. Intravesical therapy for urothelial carcinoma of the urinary bladder: a critical review. *Int Braz J Urol* 2009;35(6):640–50; discussion 651.
- Nakagawa R, Nohara T, Naito R, Kadomoto S, Iwamoto H, Yaegashi H, Kawaguchi S, Shigehara K, Izumi K, Kadono Y, Mizokami A. Intravesical BCG therapy with photodynamic diagnosis-guided transurethral resection of bladder tumors improves recurrence-free survival. *Photodiagnosis Photodyn Ther*. 2023;42:103574.
- Zheng B, Liu Z, Wang H, Sun L, Lai WF, Zhang H, Wang J, Liu Y, Qin X, Qi X, Wang S, Shen Y, Zhang P, Zhang D. R11 modified tumor cell membrane nanovesicle-camouflaged nanoparticles with enhanced targeting and mucus-penetrating efficiency for intravesical chemotherapy for bladder cancer. *J Control Release*. 2022;351:834–46.
- Lavelle J, Meyers S, Ramage R, Bastacky S, Doty D, Apodaca G, Zeidel ML. Bladder permeability barrier: recovery from selective injury of surface epithelial cells. *Am J Physiol Ren Physiol*. 2002;283(2):F242–53.
- Zhang P, Wu G, Zhang D, Lai WF. Mechanisms and strategies to enhance penetration during intravesical drug therapy for bladder cancer. *J Control Release*. 2023;354:69–79.
- Fraire JC, Guix M, Hortelao AC, Ruiz-González N, Bakenecker AC, Ramezani P, Hinnekens C, Sauvage F, De Smedt SC, Braeckmans K, Sánchez S. Light-Triggered mechanical disruption of extracellular barriers by swarms of Enzyme-Powered nanomotors for enhanced delivery. *ACS Nano*. 2023;17(8):7180–93.
- Yang S, Han G, Chen Q, Yu L, Wang P, Zhang Q, Dong J, Zhang W, Huang J. Au-Pt nanoparticle formulation as a radiosensitizer for radiotherapy with dual effects. *Int J Nanomed*. 2021;16:239–48.

9. Chen Y, Gonçalves JM, Ferrer Campos R, Villa K. Dual-Energy integration in photoresponsive micro/nanomotors: from strategic design to biomedical applications. *Small*. 2025;21(6):e2410901.
10. Amiri Z, Hasani A, Abedini F, Malek M, Madaah Hosseini HR. Urease-Powered black TiO₂ Micromotors for photothermal therapy of bladder Cancer. *ACS Appl Mater Interfaces*. 2024;16(3):3019–30.
11. Zheng Y, Zhao H, Cai Y, Jurado-Sánchez B, Dong R. Recent advances in One-Dimensional micro/nanomotors: fabrication, propulsion and application. *Nanomicro Lett*. 2022;15(1):20.
12. Chen S, Sun X, Fu M, Liu X, Pang S, You Y, Liu X, Wang Y, Yan X, Ma X. Dual-source powered nanomotor with integrated functions for cancer phototheranostics. *Biomaterials*. 2022;288:121744.
13. Hameed S, Zhang M, Bhattarai P, Mustafa G, Dai Z. Enhancing cancer therapeutic efficacy through ultrasound-mediated micro-to-nano conversion. *Wiley Interdiscip Rev Nanomed Nanobiotechnol*. 2020;12(3):e1604.
14. Naikwadi N, Paul M, Biswas S, Chitlange S, Wavhale R. Self-propelling, protein-bound magnetic nanobots for efficient in vitro drug delivery in triple negative breast cancer cells. *Sci Rep*. 2024;14(1):31547.
15. Liu L, Mo H, Wei S, Rafferty D. Quantitative analysis of Urea in human urine and serum by ¹H nuclear magnetic resonance. *Analyst*. 2012;137(3):595–600.
16. Yang N, Xiao W, Song X, Wang W, Dong X. Recent advances in tumor microenvironment hydrogen Peroxide-Responsive materials for Cancer photodynamic therapy. *Nanomicro Lett*. 2020;12(1):15.
17. Gan N, Wakayama C, Inubushi S, Kunihisa T, Mizumoto S, Baba M, Tanino H, Ooya T. Size dependency of selective cellular uptake of Epigallocatechin Gallate-modified gold nanoparticles for effective radiosensitization. *ACS Appl Bio Mater*. 2022;5(1):355–65.
18. Yu K, Kelly KL, Sakai N, Tatsuma T. Morphologies and surface plasmon resonance properties of monodisperse bumpy gold nanoparticles. *Langmuir*. 2008;24(11):5849–54.
19. Salatin S, Maleki Dizaj S, Yari Khosroushahi A. Effect of the surface modification, size, and shape on cellular uptake of nanoparticles. *Cell Biol Int*. 2015;39(8):881–90.
20. Riley RS, Day ES. Gold nanoparticle-mediated photothermal therapy: applications and opportunities for multimodal cancer treatment. *Wiley Interdiscip Rev Nanomed Nanobiotechnol*. 2017;9(4). <https://doi.org/10.1002/wnan.1449>
21. Patiño T, Feiner-Gracia N, Arqué X, Miguel-López A, Jannasch A, Stumpp T, Schäffer E, Albertazzi L, Sánchez S. Influence of enzyme quantity and distribution on the Self-Propulsion of Non-Janus Urease-Powered micromotors. *J Am Chem Soc*. 2018;140(25):7896–903.
22. Connor DM, Broome AM. Gold nanoparticles for the delivery of Cancer therapeutics. *Adv Cancer Res*. 2018;139:163–84.
23. Wang L, Guo T, Lu Q, Yan X, Zhong D, Zhang Z, Ni Y, Han Y, Cui D, Li X, Huang L. Sea-urchin-like Au nanocluster with surface-enhanced Raman scattering in detecting epidermal growth factor receptor (EGFR) mutation status of malignant pleural effusion. *ACS Appl Mater Interfaces*. 2015;7(1):359–69.
24. Wu J, Qin K, Yuan D, Tan J, Qin L, Zhang X, Wei H. Rational design of Au@Pt multibranch nanostructures as bifunctional nanozymes. *ACS Appl Mater Interfaces*. 2018;10(15):12954–9.
25. Mamonova DV, Vasileva AA, Petrov YV, Koroleva AV, Danilov DV, Kolesnikov IE, Bikbaeva GI, Bachmann J, Manshina AA. Single step Laser-Induced deposition of plasmonic Au, Ag, Pt Mono-, Bi- and Tri-Metallic nanoparticles. *Nanomaterials (Basel)*. 2021;12(1):146.
26. Ma X, et al. Enzyme-powered Hollow mesoporous janus nanomotors. *Nano Lett*. 2015;15:7043–50.
27. Dunderdale G, Ebbens S, Fairclough P, Howse J. Importance of particle tracking and calculating the mean-squared displacement in distinguishing nanopropulsion from other processes. *Langmuir*. 2012;28(30):10997–1006.
28. Isono M, Okubo K, Asano T, Sato A. Inhibition of checkpoint kinase 1 potentiates anticancer activity of gemcitabine in bladder cancer cells. *Sci Rep*. 2021;11(1):10181.
29. Kimura E, Kawano Y, Todo H, Ikarashi Y, Sugibayashi K. Measurement of skin permeation/penetration of nanoparticles for their safety evaluation. *Biol Pharm Bull*. 2012;35(9):1476–86.
30. Chai J, Yin S, Feng W, Zhang T, Ke C. The role of Hypoxia-inducible Factor-1 in bladder Cancer. *Curr Mol Med*. 2024;24(7):827–34.
31. Wang R, Du N, Jin L, Chen W, Ma Z, Zhang T, Xu J, Zhang W, Wang X, Li M. Hyaluronic acid modified Au@SiO₂@Au nanoparticles for photothermal therapy of genitourinary tumors. *Polym (Basel)*. 2022;14(21):4772.
32. Tang J, Jiang X, Wang L, Zhang H, Hu Z, Liu Y, Wu X, Chen C. Au@Pt nanostructures: a novel photothermal conversion agent for cancer therapy. *Nanoscale*. 2014;6(7):3670–8.
33. Lin H, Gao S, Dai C, Chen Y, Shi JA, Two-Dimensional. Biodegradable Niobium Carbide (MXene) for Photothermal Tumor Eradication in NIR-I and NIR-II Biowindows. *J Am Chem Soc*. 2017;139(45):16235–16247. <https://doi.org/10.1021/jacs.7b07818>. Epub 2017 Nov 2. Erratum in: *J Am Chem Soc*. 2020;142(23):10567.
34. Lyu Y, Zeng J, Jiang Y, Zhen X, Wang T, Qiu S, Lou X, Gao M, Pu K. Enhancing both biodegradability and efficacy of semiconducting polymer nanoparticles for photoacoustic imaging and photothermal therapy. *ACS Nano*. 2020;14(2):1801–10.
35. Guo L, Liu W, Niu G, Zhang P, Zheng X, Jia Q, Zhang H, Ge J, Wang P. Polymer nanoparticles with high photothermal conversion efficiency as robust photoacoustic and thermal theranostics. *J Mater Chem B*. 2017;5(15):2832–9.
36. Zhou J, Jiang Y, Hou S, Upputuri PK, Wu D, Li J, Wang P, Zhen X, Pramanik M, Pu K, Duan H. Compact plasmonic blackbody for Cancer theranosis in the Near-Infrared II window. *ACS Nano*. 2018;12(3):2643–51.
37. Ayala-Orozco C, Urban C, Knight MW, Urban AS, Neumann O, Bishnoi SW, Mukherjee S, Goodman AM, Charron H, Mitchell T, Shea M, Roy R, Nanda S, Schiff R, Halas NJ, Joshi A. Au Nanomatryoshkas as efficient near-infrared photothermal transducers for cancer treatment: benchmarking against nanoshells. *ACS Nano*. 2014;8(6):6372–81.
38. Liu T, Zhang M, Liu W, Zeng X, Song X, Yang X, Zhang X, Feng J. Metal Ion/Tannic acid assembly as a versatile photothermal platform in engineering multimodal nanotheranostics for advanced applications. *ACS Nano*. 2018;12(4):3917–27.
39. Zhang J, Yang C, Zhang R, Chen R, Zhang Z, Zhang W, Peng SH, Chen X, Liu G, Hsu CS, Lee CS. Biocompatible D-A semiconducting polymer nanoparticle with Light-Harvesting unit for highly effective photoacoustic imaging guided photothermal therapy. *Adv Funct Mater*. 2017;27(13):1605094.
40. Qin X, Wang H, Xu W, Zheng B, Zhang H, Zhang Q, Liu Y, Liu Z, Sun L, Mou Y, Yao C, Zheng W, Chen Y, Wang C, Zhou X, Shen Y, Zhang P, Zhang D. A Selective-Tumor-Penetrating strategy via unidirectional direct transfer for intravesical therapy of bladder Cancer. *J Med Chem*. 2024;67(6):4904–15.
41. Ye R, Zhang Y, Chen Y, Tang L, Wang Q, Wang Q, Li B, Zhou X, Liu J, Hu J. Controlling shape and plasmon resonance of Pt-Etched Au@Ag nanorods. *Langmuir*. 2018;34(20):5719–27.
42. Feng L, Gao G, Huang P, Wang X, Zhang C, Zhang J, Guo S, Cui D. Preparation of Pt ag alloy Nanoisland/graphene hybrid composites and its high stability and catalytic activity in methanol electro-oxidation. *Nanoscale Res Lett*. 2011;6(1):551.

Publisher's note

Springer Nature remains neutral with regard to jurisdictional claims in published maps and institutional affiliations.